AL 6061-T6 - Elastomer Impact Simulations

PI: Jacob Fish
Research Associate: Coglar Oskay
PhD student: Rong Fan

Program Monitor: Roshdy Barsoum

June 21, 2005

Abstract

The behavior of the layered AL 6061-T6 - Elastomer (ERC) structure is investigated using 3D numerical simulations on different configurations shown in Fig. 4. The AL 6061-T6 is modeled as an elastic-plastic material using the Johnson Cook plasticity model; the ERC is modeled as a hyperelastic-viscoelastic material using the pressure and temperature dependent constitutive law (Nemat-Nasser, 2004). The two material models were incorporated into ABAQUS and validated against experimental data. Numerical simulations confirmed the stiffening behavior of the ERC at high strain rates. The pressure transmitted at the interface between the AL 6061-T6 and ERC has been found to be governed by the ratio of specific acoustic resistance of the two materials. Numerical simulations have been found to be in good agreement with theoretical estimates.

Material Properties

The AL 6061-T6 is modeled as an elastic-plastic material with Von-Mises type yield function using the Johnson Cook plasticity model:

$$\bar{\sigma} = \left[A + B\left(\bar{\varepsilon}^{pl}\right)^{n} \right]\left[1 + C\ln\left(\frac{\dot{\bar{\varepsilon}}^{pl}}{\dot{\varepsilon}_0} \right) \right]\left(1 - \hat{\theta}^{m}\right)$$

where $\bar{\sigma}$ is the yield stress, $\bar{\varepsilon}^{pl}$ and $\dot{\bar{\varepsilon}}^{pl}$ are the equivalent plastic strain and plastic strain rate, respectively; A, B, n, m and $\dot{\varepsilon}_0$ are material parameters measured at or below the transition temperature; $\hat{\theta}$ is a nondimensional temperature, defined as:

$$\hat{\theta} \equiv \begin{cases} 0 & for \quad \theta < \theta_{transition} \\ \left(\theta - \theta_{transition}\right)/\left(\theta_{melt} - \theta_{transition}\right) & for\ \theta_{transition} \le \theta \le \theta_{melt} \\ 1 & for \quad \theta > \theta_{melt} \end{cases}$$

where θ is the current temperature; θ_{melt} the melting temperature, and $\theta_{transition}$ the transition temperature. The transition temperature is defined as the temperature at which

the transition from ductile to brittle fracture takes place. The Johnson Cook coefficients are summarized in Table 1. The model is incorporated into ABAQUS and validated against the experimental data. Figure 1 shows the experimental and numerically simulated isothermal uniaxial true-stress true-strain curves at 71^0F for the strain rates of 2500/s and 0.001/s.

Table 1: Johnson Cook Coefficients

A	B	C	n	M	$\dot{\varepsilon}_0$	θ_{melt}	$\theta_{transition}$
289.6MPa	203.4MPa	0.011	0.35	1.34	$1.0\,s^{-1}$	925.37K	294.26K

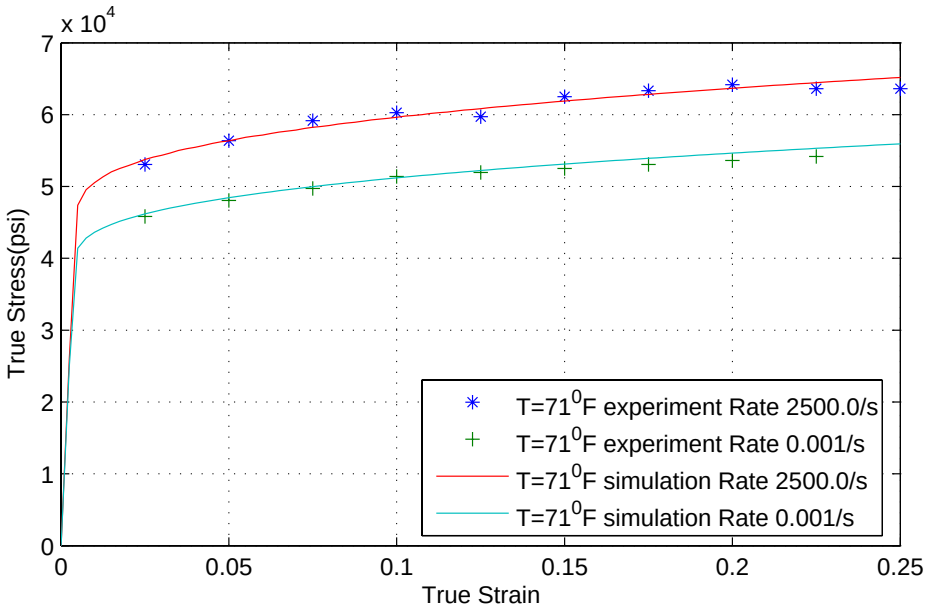

Figure 1: Isothermal stress-strain curves at the strain rates of 2500/s and 0.001/s

The elastomer (ERC) is modeled using the pressure and temperature dependent hyperelastic-viscoelastic constitutive law (Nemat-Nasser (2004)[1]). The Mooney-Rivlin potential is assumed and viscous effects were modeled using an exponential series representation. The relaxation curve is given by:

$$G(t,\tau) = G_\infty \left(1 + \sum_{n=1}^{6} p_n \exp\left[-\frac{\xi(t)-\xi(\tau)}{q_n}\right]\right)\frac{T}{T_0}$$

where,

$$\xi(t) = \int_0^t \frac{d\tau}{a\left(T - C_d \varepsilon_{ii}\right)}$$

in which, ε_{ii} is the hydrostatic strain. The shift function is given by

[1] Nemat-Nasser, S., (2004). "Experimental characterization of polyurea with constitutive modeling and simulations," *presentation at ERC ACTD Workshop*, Massachusetts Institute of Technology.

$$\log\left[a(T)\right] = \frac{A(T - T_0)}{B + T - T_0}$$

The material parameters are summarized in Table 2.

Table 2: Polyurea material parameters

p_n:	397.7	0.496	4.804e-3	8.856e-5	3.342e-6	1.671e-7
q_n:	0.291	0.326	0.491	0.86	1.136	1.712
G_∞:	66 MPa	A:	-10	B:	107.54 K	
C_d:	265 K	Poisson υ:[1]	0.484			

The model is incorporated into ABAQUS and validated against the experimental data provided by Knauss (2004)[2] and Nemat-Nasser (2004)[3]. Figure 2 shows the experimental and numerically simulated master relaxation curves for the elastomer. Figure 3 shows the experimental and numerically simulated confined stress-strain curves at the 273 K with a strain rate of 2100/s. The Poisson ratio used in the simulation was 0.48993, so that the stiffening factor due to confinement is 17.

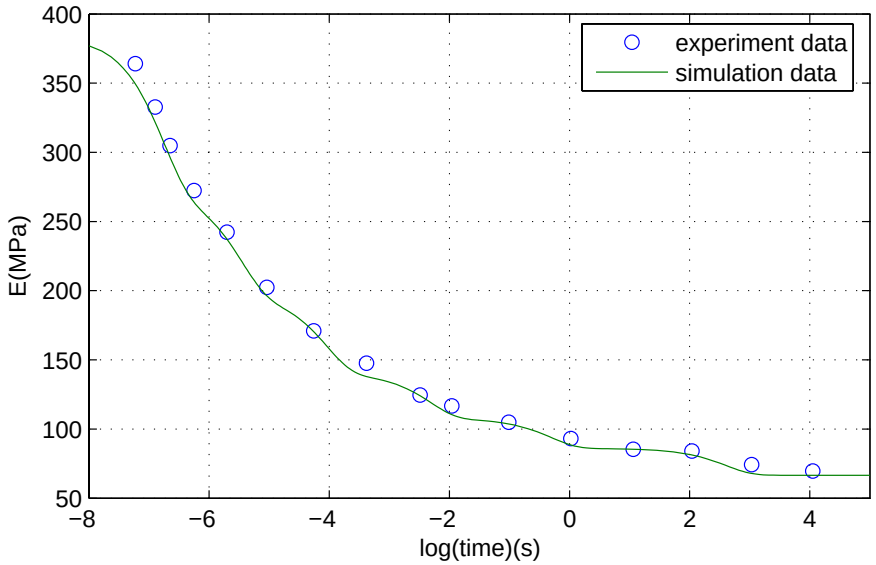

Figure 2: Master relaxation curve

[1] Rod Clifton and Tonia Jiao, (2004). "High strain rate response of elastomers", *presentation at ERC ACTD Workshop*, Massachusetts Institute of Technology.
[2] W.G. Knauss, (2004). "Separate and combined time-temperature and time-pressure interactions". *presentation at ERC ACTD Workshop*, Massachusetts Institute of Technology.
[3] Nemat-Nasser, S., (2004). "Experimental characterization of polyurea with constitutive modeling and simulations," *presentation at ERC ACTD Workshop*, Massachusetts Institute of Technology.

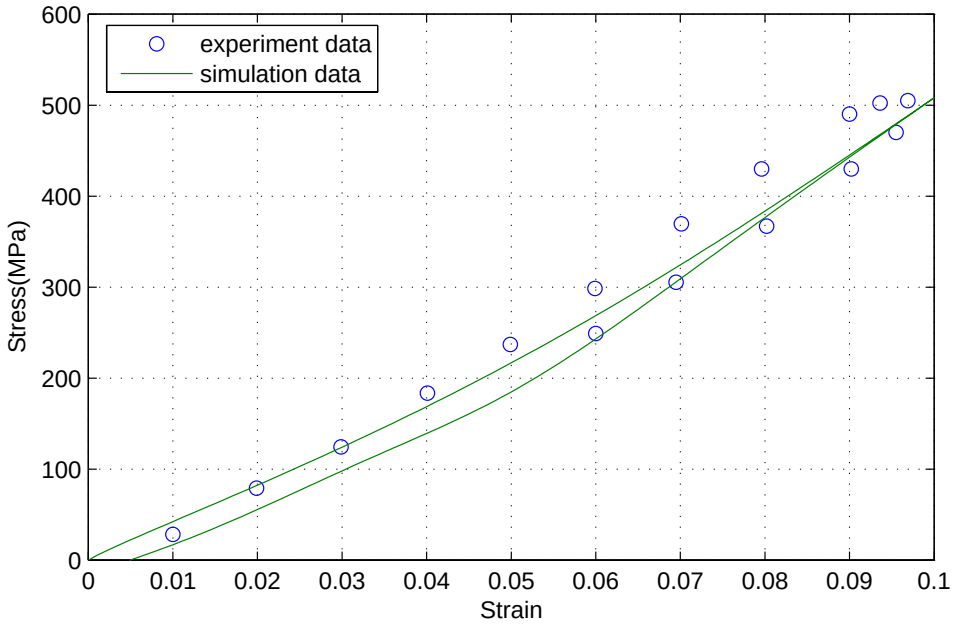

Figure 3: Confined stress-strain curve at a strain rate of 2100/s

Numerical Simulation Setup

Several simulations were performed for the AL 6061-T6 - ERC specimens with different configurations shown Fig.4. The thickness of the specimens is 101.6mm (4in), and the diameter is 127mm (5in). By exploiting the symmetry of geometry, loading and boundary condition, the 4-node bilinear axisymmetric quadrilateral elements with reduced integration and hourglass control was used in these simulations.

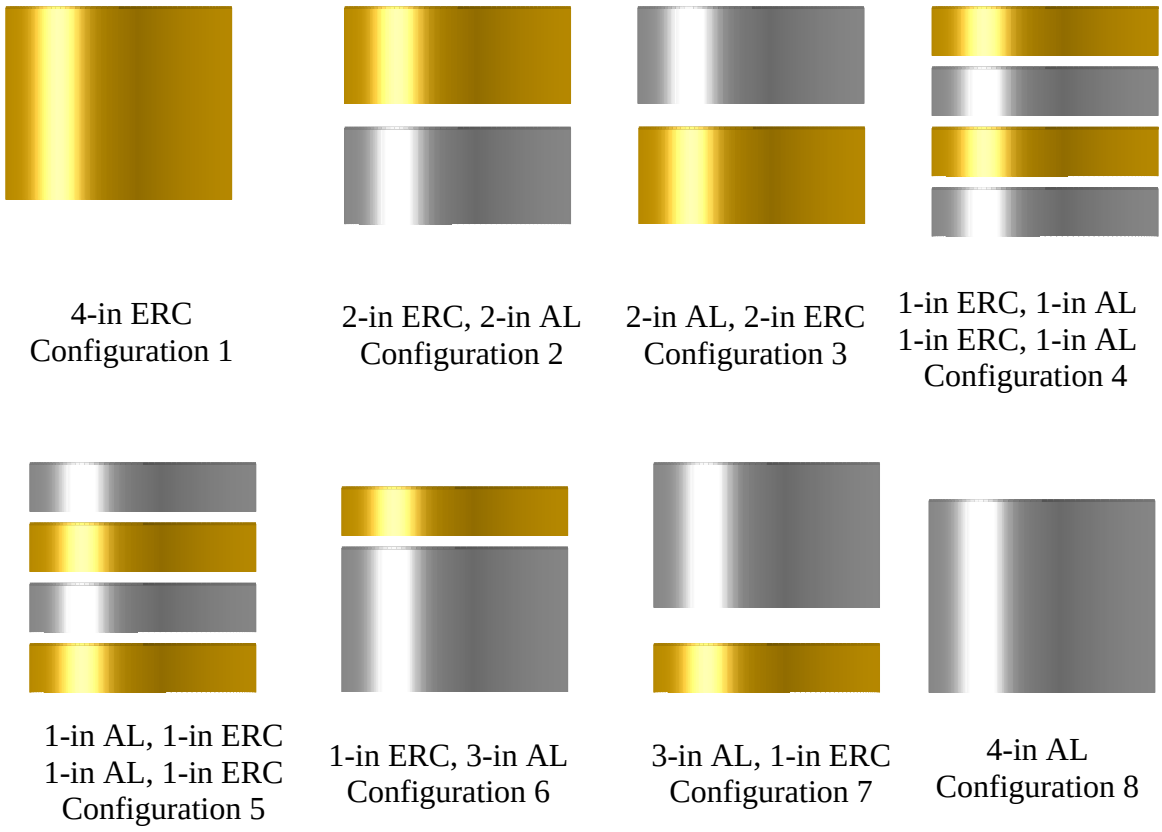

Figure 4: Specimens Configurations

The specimens were subjected to two impact velocities of 50 and 500 m/s (average velocity) as shown in Fig. 5. The assumed boundary conditions are also illustrated in Fig. 5. Fig. 6 shows the variation of the applied velocity profiles with time.

For the above applied velocities, the maximum strain rates in the ERC for the Configuration 1 were 772/s and 7754/s, respectively.

All analyses were conducted under isothermal conditions with a temperature of 294.82K.

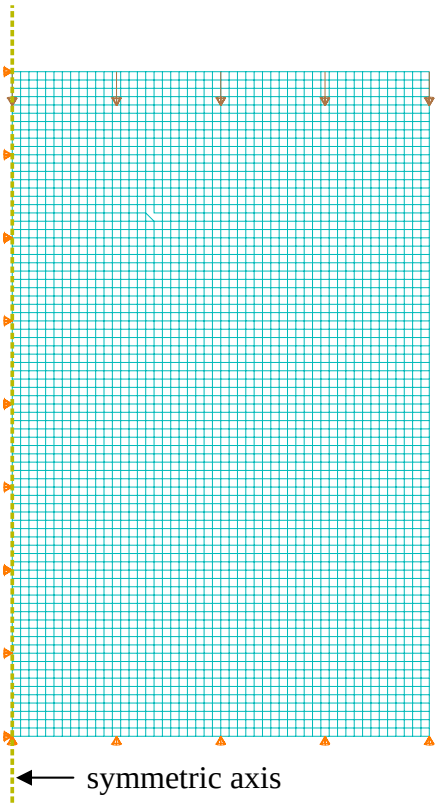

Figure 5: FE mesh with B.C. and loading

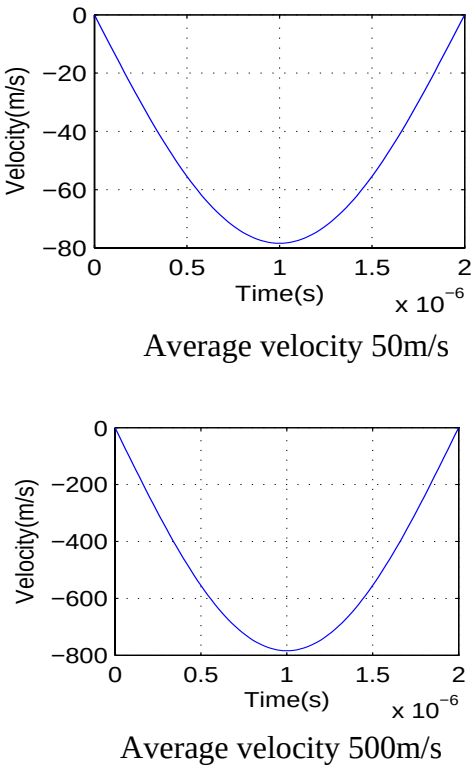

Figure 6: Applied impact velocity

Results and Discussion

The primary objective of the numerical simulations is to investigate the effect of different configurations on the pressure at the elastomer – aluminum interface. For the impact velocity of 50m/s, Figs.7a—7c show the axial pressure distribution at the top of the specimen at different time instances, before the pressure reaches its peak at the top (Fig. 7a), when the pressure reaches the peak value at the top (Fig. 7b), and after the wave reaches the highest value at the top (Fig. 7c). Similarly, Figs. 7d—7f correspond to the time instances, before the wave peak reaches the bottom, when the wave peak reaches the bottom, and after the wave peak reaches the bottom, respectively. Figs. 8a—8f display the axial pressure distribution at the top and bottom for the impact velocity of 500m/s. The pressure distribution along the radial direction is quite uniform at the beginning of impact. However, as the wave travels deep into the specimen, the pressure looses its uniformity due to three-dimensional effects. The wave propagating from the free surface interacts with the axial compressive wave, which destroys the pressure uniformity along the radial direction. This is illustrated in the snapshot of the pressure contours for the Configuration 1 with the impact velocity of 50m/s (Fig. 9).

For the Configuration 1 with applied impact average velocities 50m/s and 500m/s, Figs. 10 and 11 display the pressure distributions along the central axis at five different time instances when the pressure reaches the highest value: at the top, 1/4 the length from the top, 1/2 the length from the top, 3/4 the length from the top and at the bottom. The maximum pressures at these time instances are given in Tables 3a and 3b for the applied impact average velocities of 50m/s and 500m/s, respectively. It can be seen from Table 3a that the pressure drops significantly in the first 1/4 of the length. Also from Table 3a we may notice that the time intervals for the wave traveling between the four stations along the centerline are increasing. This means that the wave velocity is decreasing with time, due to viscous effects in ERC. The average longitudinal wave velocity is 1311m/s for the impact average velocity of 50m/s. Moreover, the viscosity of ERC is in part responsible for the change in the shape of the compressive wave, as it can be seen from Fig. 10. On the other hand, for the impact velocity of 500m/s, the compressive wave maintains the same shape (see Fig. 11) as it travels at a constant velocity of 1798m/s! The pressure loss is only 30% for the impact velocity of 500m/s as opposed to 90% loss for the impact velocity of 50m/s. We believe that this is a direct consequence of the shift function in the ERC model provided by Nemat-Nasser (2004). For the impact velocity of 500m/s, the hydrostatic strain ε_{ii} in ERC is greater than 0.3 as the wave reaches its peak. The magnitude of the shift function $\log\left[a\left(T - C_d\varepsilon_{ii}\right)\right]$ is greater than 10. This means that for impact velocity of 500m/s, when the peak of the compressive wave reaches the ERC, there is no relaxation of bulk modulus or shear modulus, due to the pressure effect in ERC.

Table 3a: Pressure amplitude for Configuration 1 with impact V=50m/s

t(μs)	1.5	20.0	39.0	58.5	79.0
Pressure(MPa)	109.26	28.96	15.28	9.38	13.26
Normalized Pressure	1.0	0.27	0.14	0.09	0.12

Table 3b: Pressure amplitude for Configuration 1 with impact V=500m/s

t(μs)	1.5	15.5	29.5	43.5	58
Pressure(MPa)	1570.68	1099.57	1102.91	1062.5	2106.41
Normalized Pressure	1.0	0.70	0.70	0.68	1.34

When the wave peak reaches the bottom, the magnitude of the pressure doubles and the reflecting wave has equal amplitude and the same sign as the incident wave.

Figs. 12 to 23 depict the pressure distributions at the AL-ERC interfaces for the Configurations 2 to 7 at three different time instances: before, at and after the peak pressure at the center reaches the corresponding interface. For the above configurations, ERC responds differently at different impact velocities. The higher the impact velocity is,

the stiffer it behaves. The pressure distribution at the top of the ERC layer for the Configurations 2, 4 and 6 is identical to the pressure distribution for the Configuration 1.

The pressure distribution for the Configuration 8 is displayed in Figs. 24 to 27 for the applied velocities of 50m/s and 500m/s. Figs. 24 and 25 show the pressure distribution along the radial direction for the five different sections: at the top, 25.4mm from the top, 50.8mm from the top, 76.2mm from the top and at the bottom. The time instances are chosen to be the time at which the pressures reach its highest value at the centers of these sections. The pressure amplitudes corresponding to Figs. 26 and 27 are summarized in Table 4a and 4b, respectively. The pressure decreases rather slowly in the aluminum as the compressive wave propagates, but the rate of decrease is more pronounced for the lower impact velocity.

Table 4a: Pressure amplitude for Configuration 8 with impact V=50m/s

t(μs)	1.0	5.5	9.5	13.5	18.0
Pressure(MPa)	1168.89	832.18	683.29	646.08	1150.66
Normalized presssure	1.0	0.71	0.58	0.55	0.98

Table 4b: Pressure amplitude for Configuration 8 with impact V=500m/s

t(μs)	1.0	5.5	10.5	15.5	20.5
Pressure(MPa)	10967.6	9712.8	8132.7	6482.4	9998.3
Normalized presssure	1.0	0.89	0.74	0.59	0.91

It is instructive to comment on how the pressures change at the interface for the Configurations 2 to 7. For example, for the Configuration 4 with the applied impact velocity of 50m/s, the maximum reflected pressure in the ERC at the center of the first interface is 54.63MPa, and the pressure transmitted to the aluminum is 55.07MPa. After the pressure wave passes the aluminum layer and is transmitted to the second layer of ERC, the pressure further decreased to 8.29MPa. This phenomenon has a theoretical explanation given below.

The longitudinal elastic wave velocity is

$$\sqrt{(K+\frac{4}{3}G)/\rho}$$

where K is the bulk modulus, G the shear modulus, and ρ the mass density. For the AL 6061-T6, the longitudinal elastic wave velocity is 6149m/s. For the impact average velocity of 50m/s, the average longitudinal wave velocity calculated from the numerical simulation is 5976m/s, which is a bit lower than the elastic wave velocity. This is expected due to some minor plastic deformation taking place in the aluminum. For the impact velocity of 500m/s, the plastic deformation is more pronounced, and the average longitudinal wave velocity drops to 5210m/s.

The ratio of pressures between the transmitted and the incident waves may be approximated using the following relation:

$$\frac{P_T}{P_I} = \frac{2\rho_T V_T}{\rho_T V_T + \rho_I V_I}$$

where P_T and P_I are the transmitted pressure and the incident pressure, respectively; ρ_T and ρ_I are the corresponding mass densities; V_T and V_I are the longitudinal wave velocities. Obviously, the above is a rough estimate since it corresponds to one-dimensional wave propagation and thus ignores three-dimensional effects. The product of the wave velocity and density is commonly known as the specific acoustic resistance. As the wave traveling in ERC arrives at the ERC-aluminum interface, the ratio of the pressure transmitted to aluminum to the incident pressure in ERC is 1.84, as computed using the above formula provided that the aluminum remains elastic and the velocity in the ERC is 1310m/s. As the wave traveling in the aluminum arrives at the aluminum-ERC interface, the ratio of the pressure transmitted to ERC to the incident pressure in the aluminum is 0.24, if the wave velocity is 5210 m/s in the aluminum. These theoretical values are in good agreement with those computed using numerical simulations. For example, when the Configuration 2 is subjected to the impact velocity of 50m/s, the pressure transmitted to the aluminum is 28.77MPa, and the incident pressure is 15.28MPa, so the ratio is 1.88. For the Configuration 3 with the impact velocity of 500m/s, the pressure transmitted to the ERC is 1846.0MPa, and the incident pressure is 7671.2MPa, so the ratio is 0.24.

In conclusion, for different impact velocities, ERC responds differently. Numerical simulations for different configurations show that ERC becomes stiffer at higher impact velocities (or impact pressures). The ratio of $\rho_{AL}V_{AL} / \rho_{ERC}V_{ERC}$ determines the pressure transmitted at the boundary between the aluminum and ERC. When compressive wave from ERC hits the aluminum layer, the wave reflects back to the ERC as a compressive wave. On the other hand, when the compressive wave from the aluminum hits the ERC, the wave reflects back to aluminum as a tensile wave.

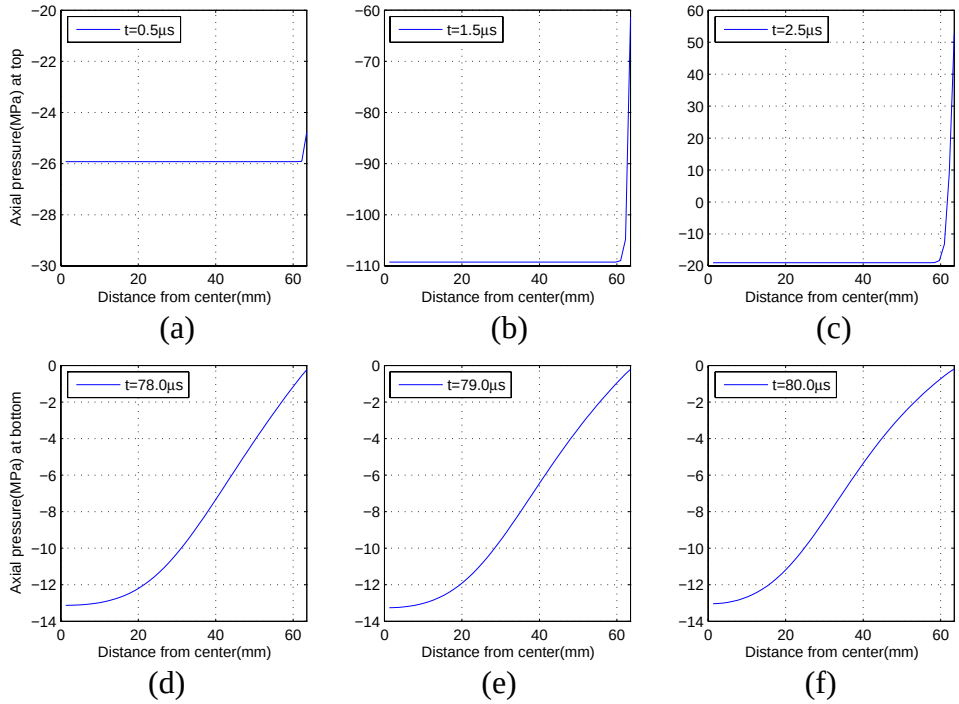

Figure 7: Pressure for Configuration 1 with applied average velocity V=50m/s

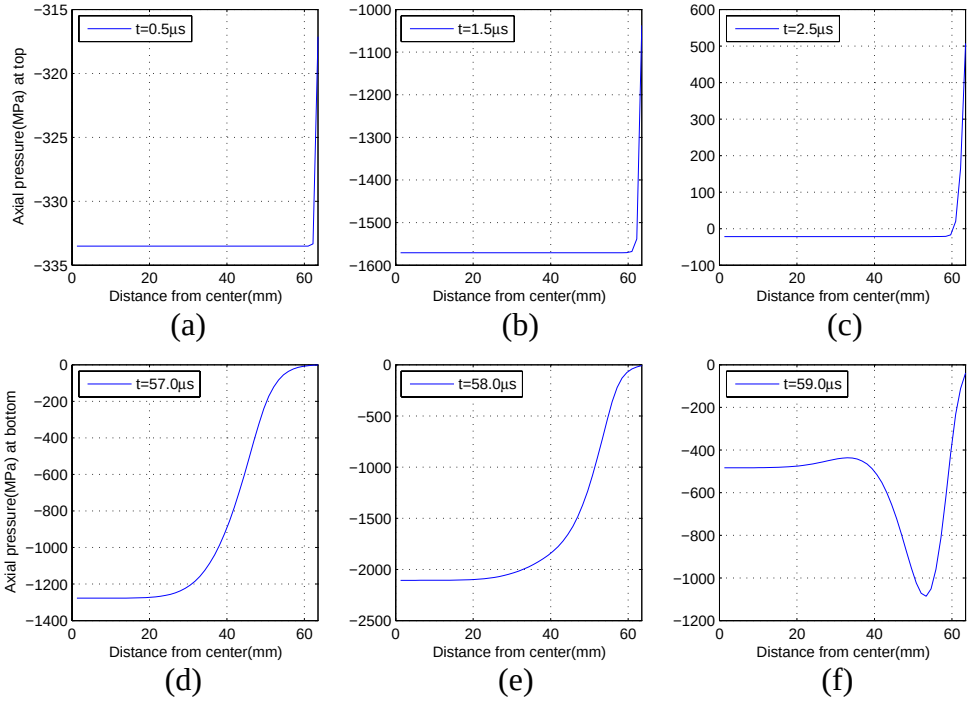

Figure 8: Pressure for Configuration 1 with applied average velocity V=500m/S

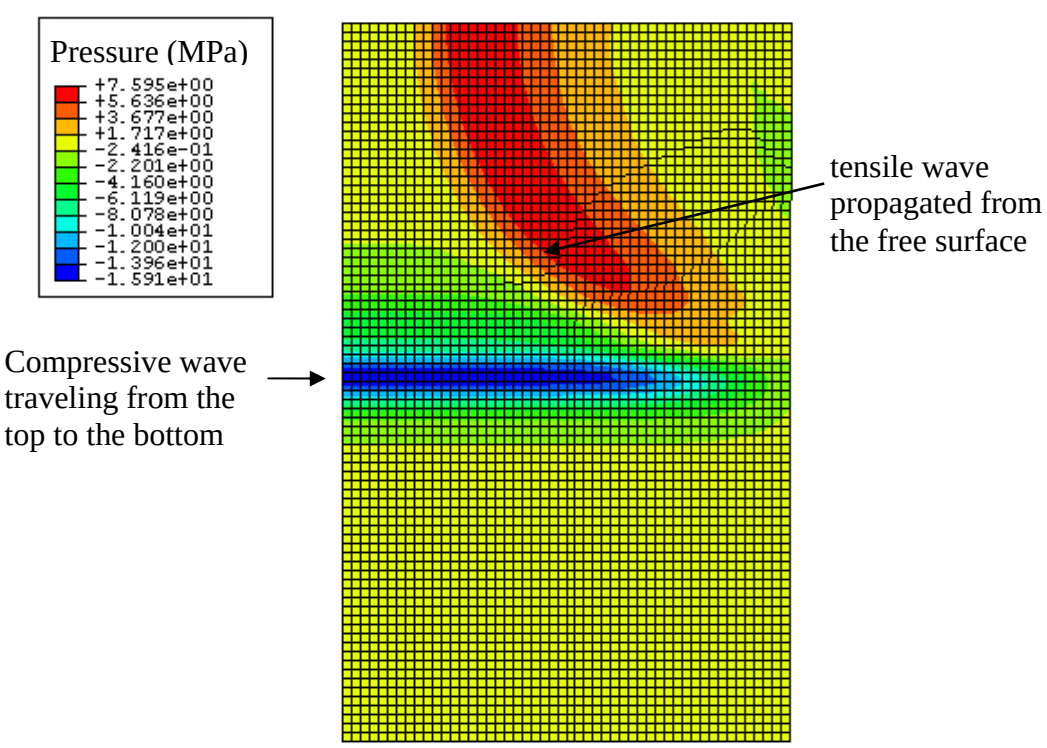

Figure. 9: Snapshot of wave propagation for Configuration 1

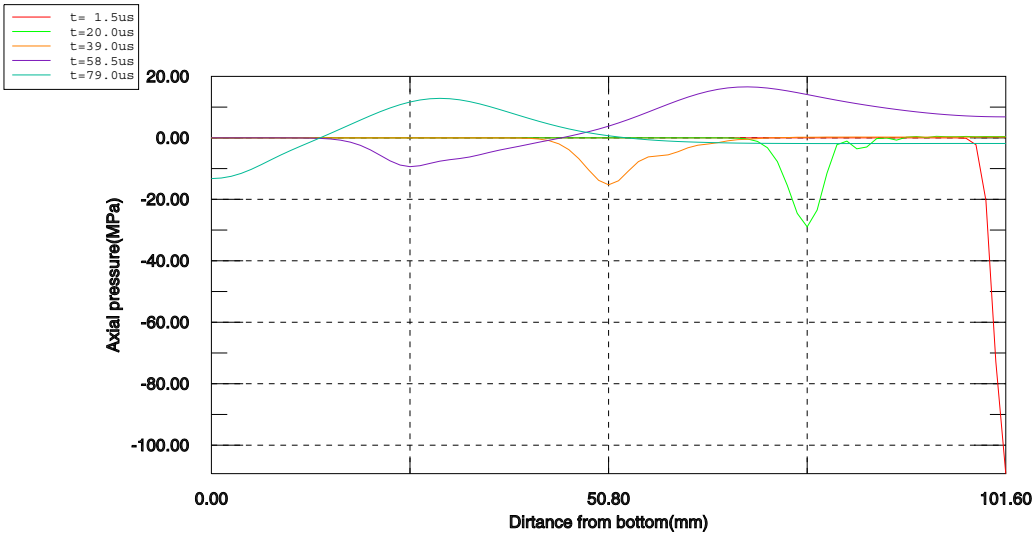

Figure 10: Pressure along the central axis for applied average velocity V=50m/s

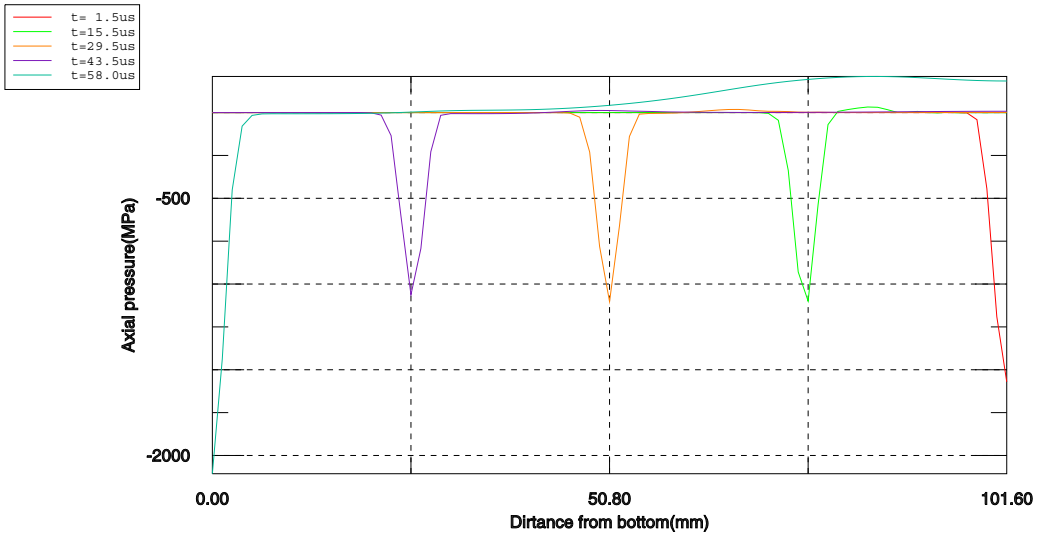

Figure 11: Pressure along the central axis for applied average velocity V=500m/s

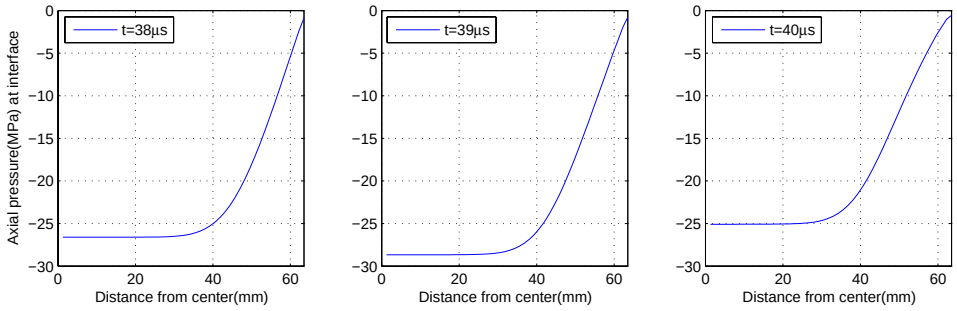

(a) (b) (c)

Figure 12: Pressure for Configuration 2 with applied average velocity V=50m/s

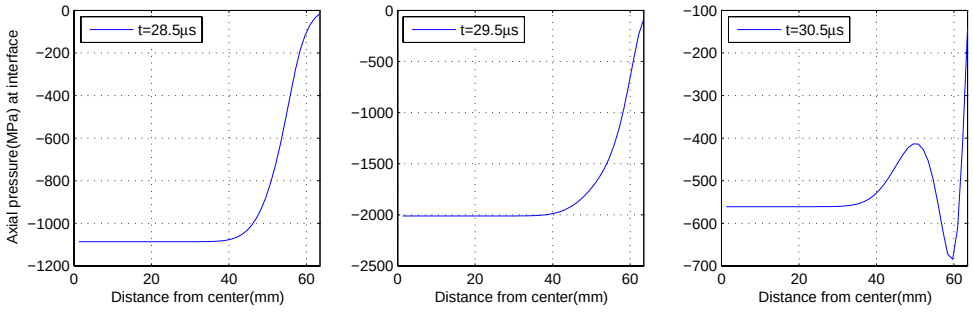

(a) (b) (c)

Figure 13: Pressure for Configuration 2 with applied average velocity V=500m/s

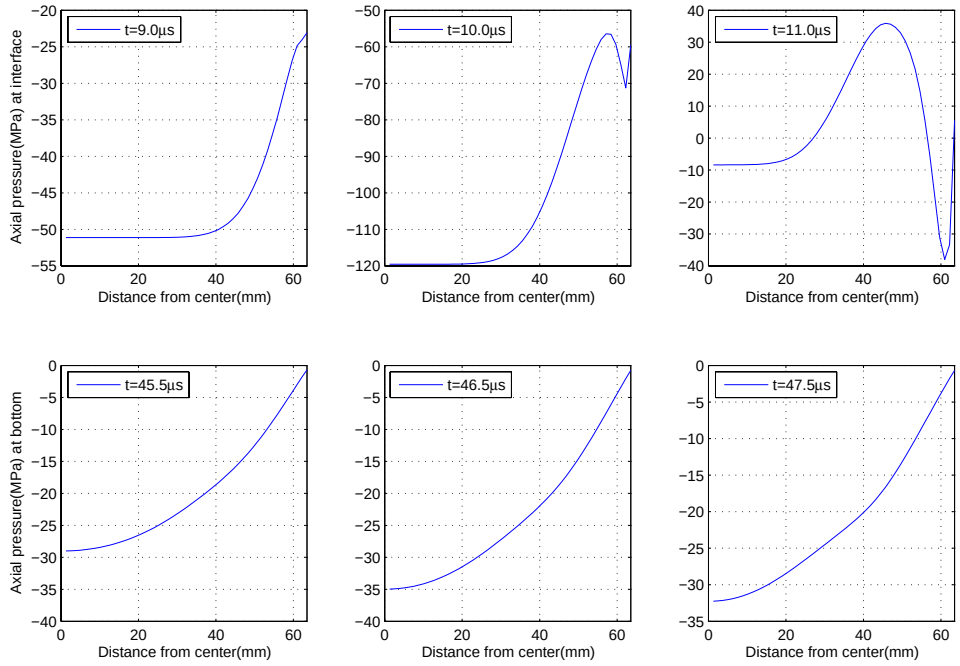

Figure 14: Pressure for Configuration 3 with applied average velocity V=50m/s

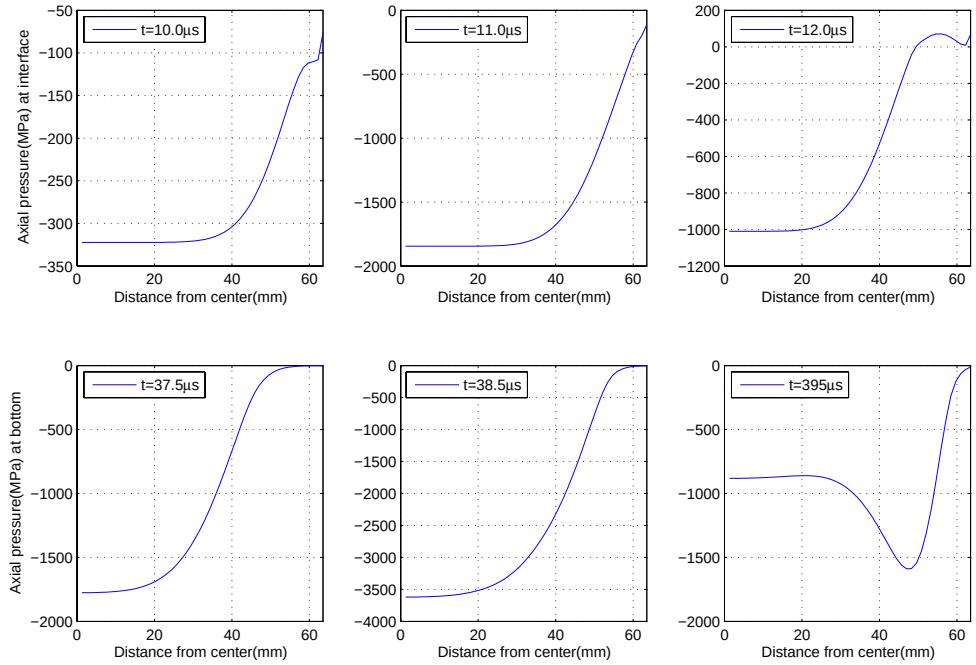

Figure 15: Pressure for Configuration 3 with applied average velocity V=500m/s

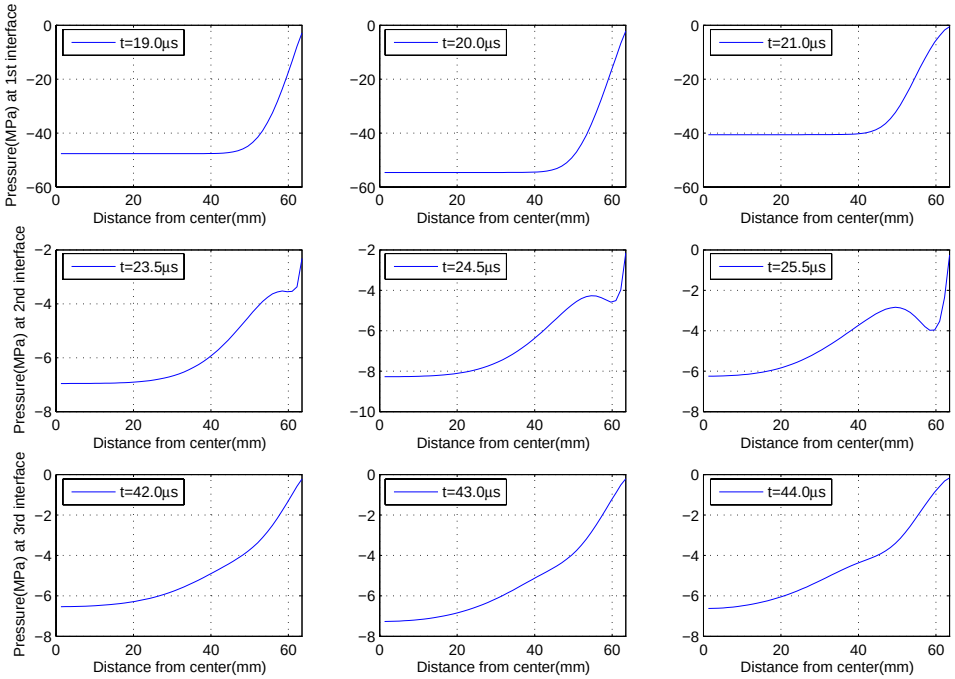

Figure 16: Pressure for Configuration 4 with applied average velocity V=50m/s

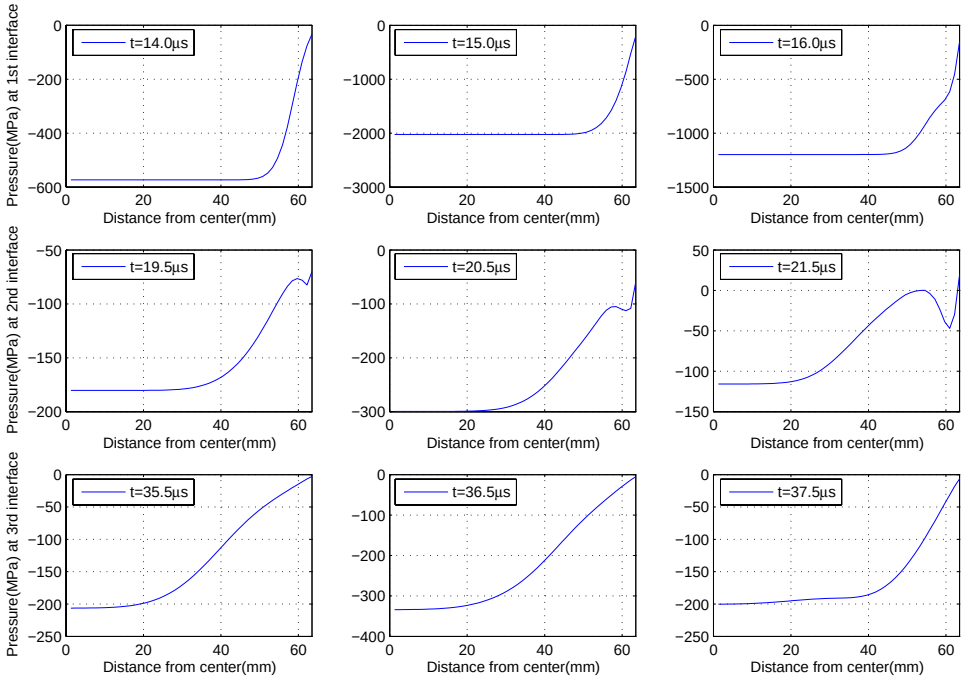

Figure 17: Pressure for Configuration 4 with applied average velocity V=500m/s

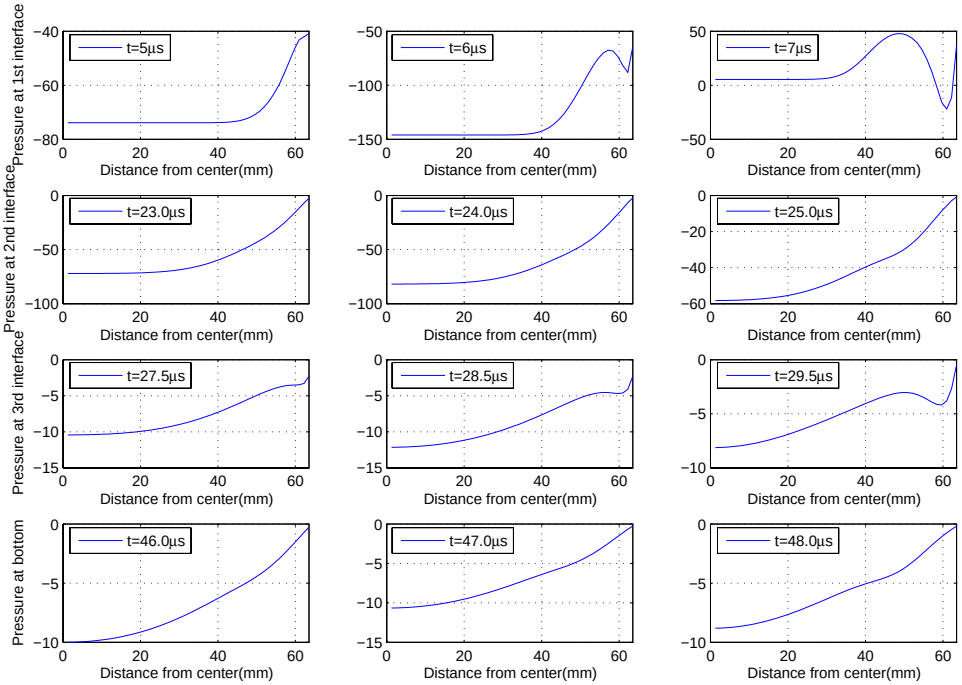

Figure 18: Pressure for Configuration 5 with applied average velocity V=50m/s

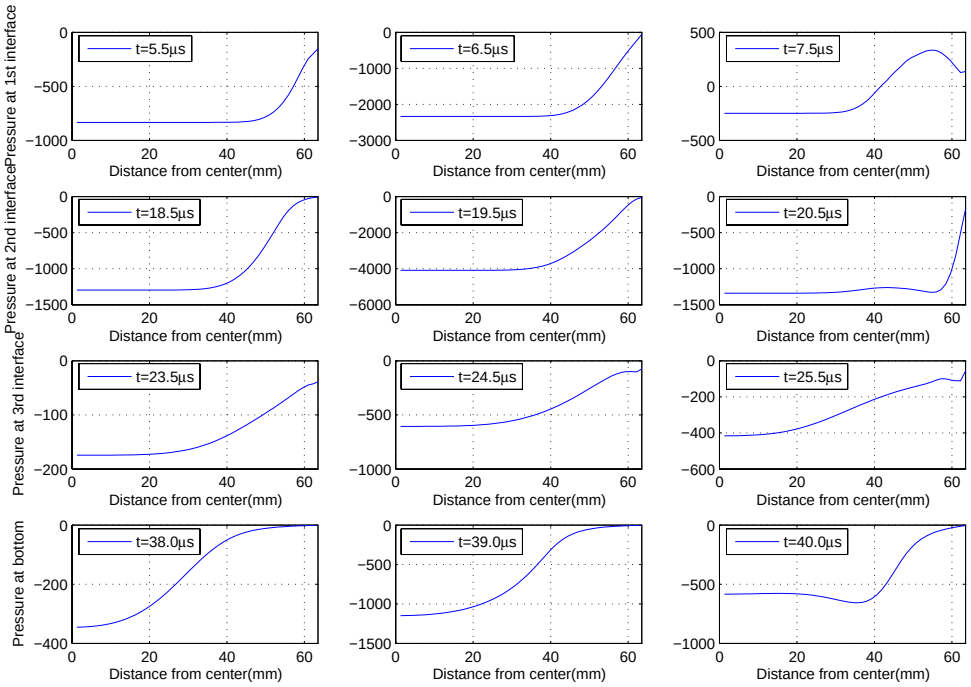

Figure 19: Pressure for Configuration 5 with applied average velocity V=500m/s

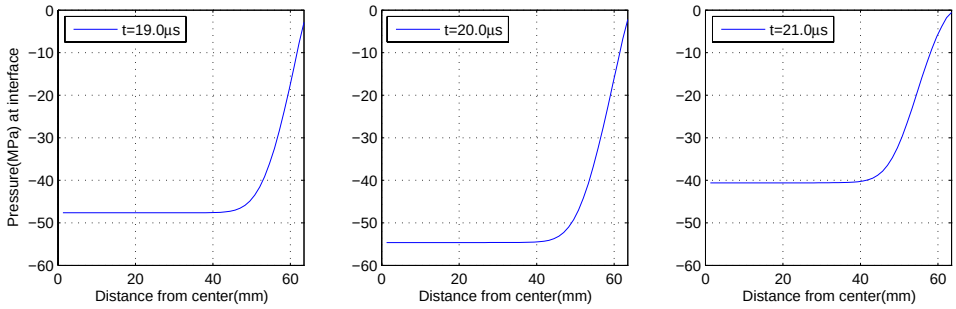

Figure 20: Pressure for Configuration 6 with applied average velocity V=50m/s

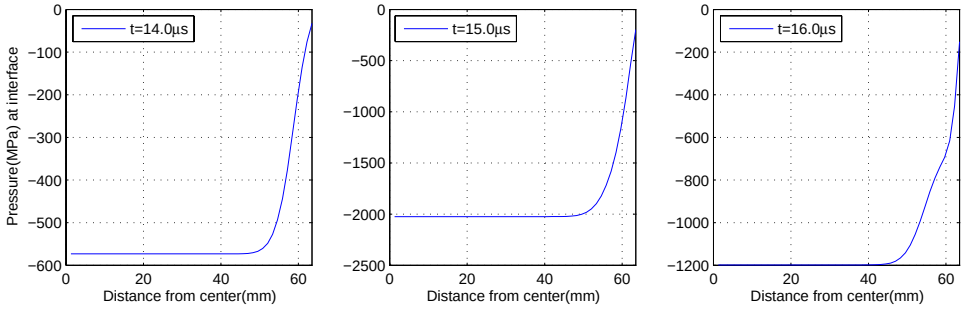

Figure 21: Pressure for Configuration 6 with applied average velocity V=500m/s

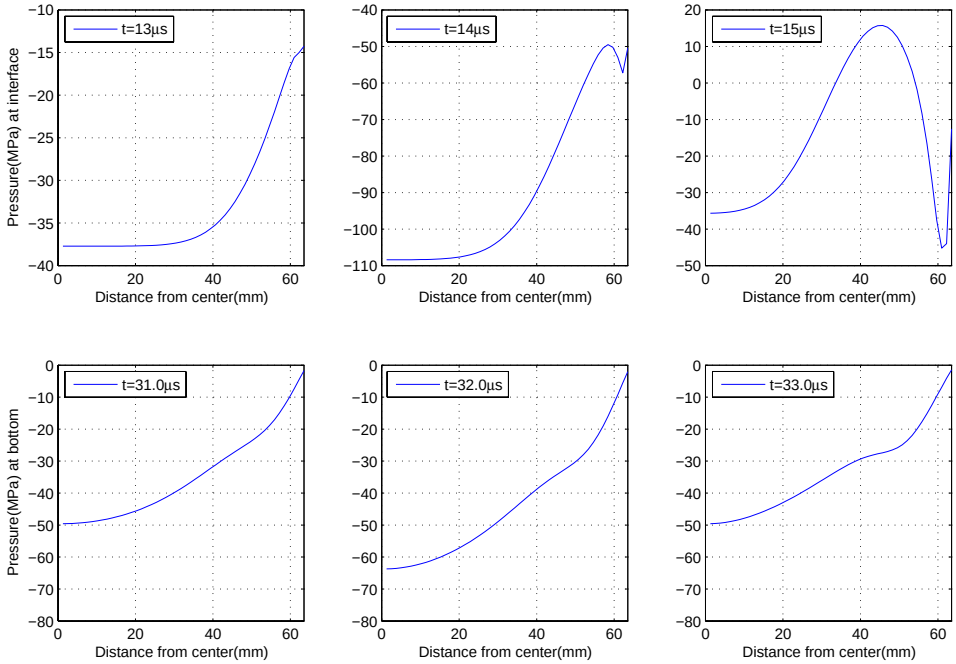

Figure 22: Pressure for Configuration 7 with applied average velocity V=50m/s

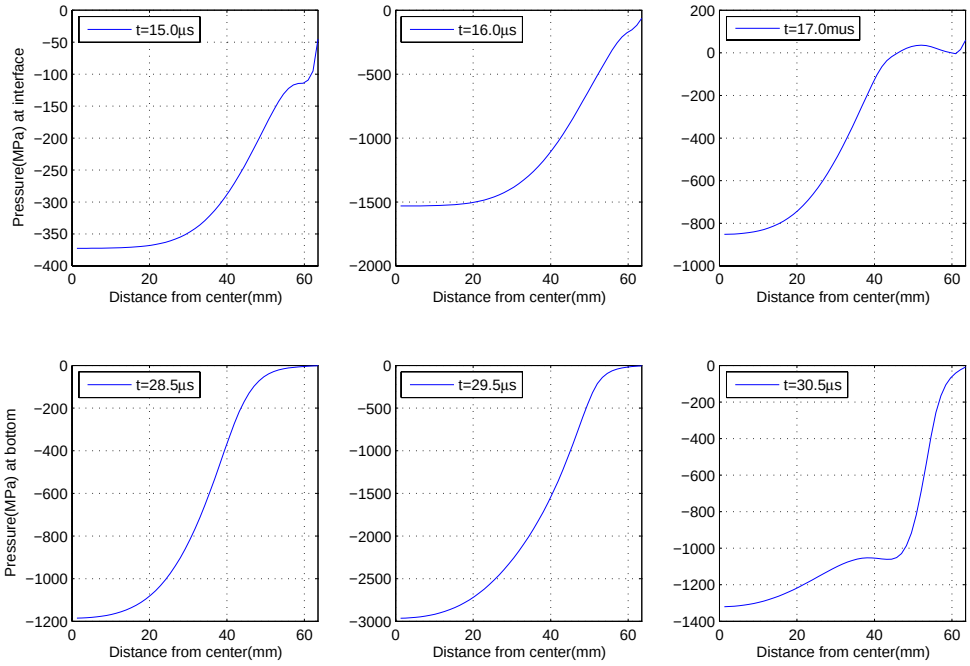

Figure 23: Pressure for Configuration 7 with applied average velocity V=500m/s

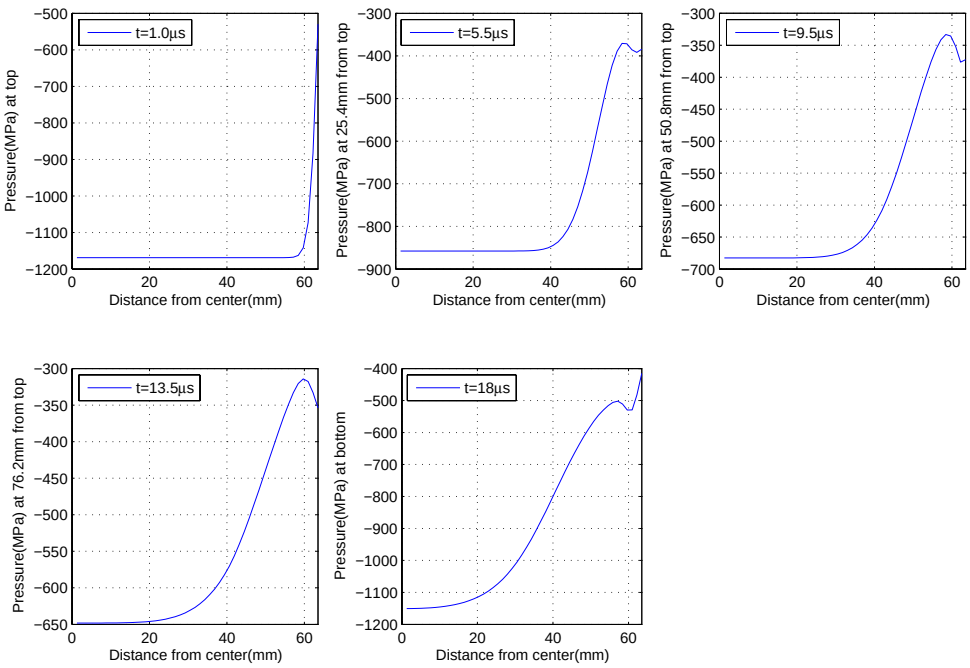

Figure 24: Pressure for Configuration 8 with applied average velocity V=50m/s

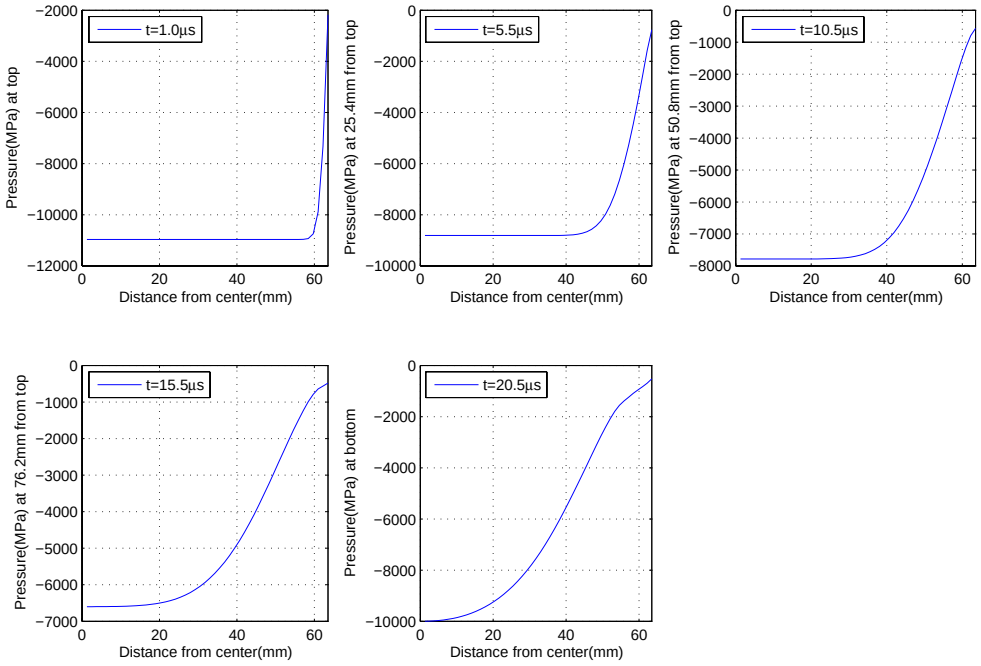

Figure 25: Pressure for Configuration 8 with applied average velocity V=500m/s

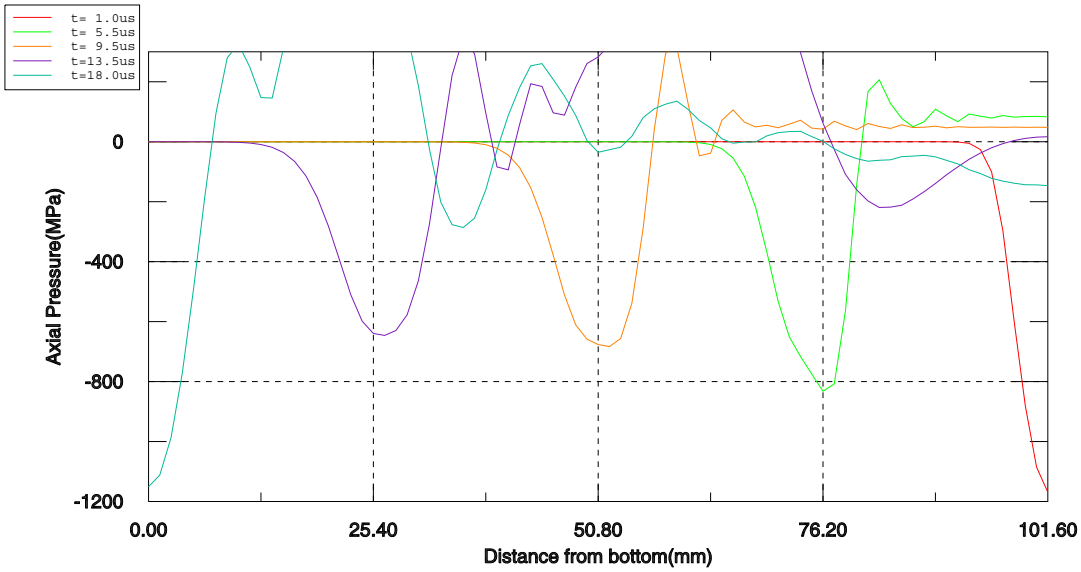

Figure 26: Pressure along the central axis for applied average velocity V=50m/s

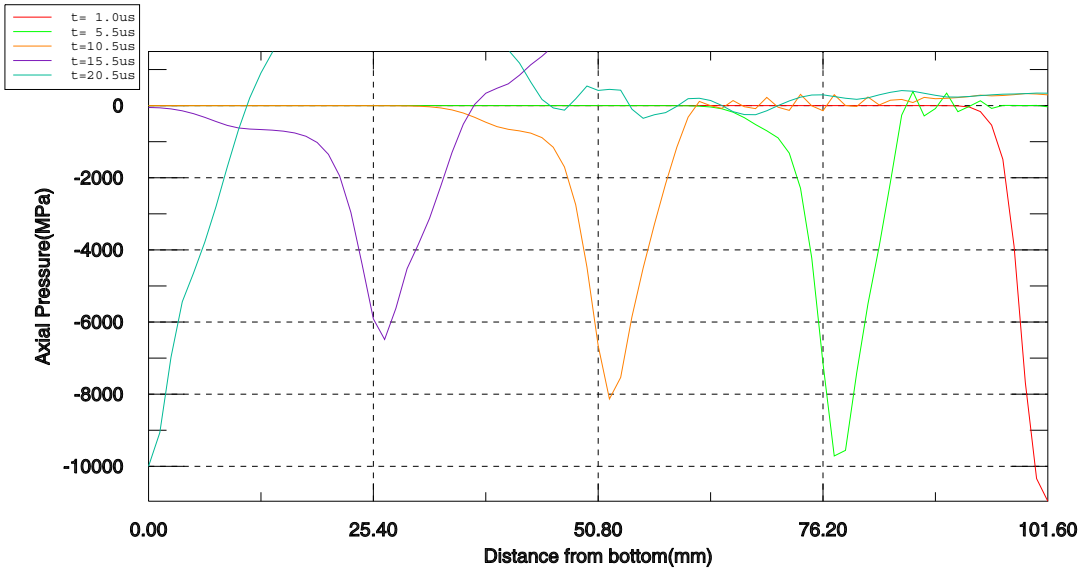

Figure 27: Pressure along the central axis for applied average velocity V=500m/s